

Tsunami source inversion using time-derivative waveform of offshore pressure records to reduce effects of non-tsunami components

Tatsuya Kubota,¹ Wataru Suzuki,¹ Takeshi Nakamura,¹ Naotaka Y. Chikasada,¹ Shin Aoi,¹ Narumi Takahashi^{1,2} and Ryota Hino³

¹National Research Institute for Earth Science and Disaster Resilience, 3-1, Tennodai, Tsukuba, Ibaraki 305-0006, Japan. E-mail: kubotatsu@bosai.go.jp

²Japan Agency for Marine-Earth Science and Technology, 3173 -25, Showa-machi, Kanazawa-ku, Yokohama, Kanagawa 236-0001, Japan

³Graduate School of Science, Tohoku University, 6-6, Aza-Aoba, Aramaki, Aoba-ku, Sendai, Miyagi 980-8678, Japan

Accepted 2018 August 17. Received 2018 August 13; in original form 2018 May 07

SUMMARY

Offshore ocean bottom pressure gauges (OBPs) are often used to estimate the spatial distribution of the initial sea-surface height associated with offshore earthquakes (the tsunami source model). However, the sensors sometimes record pressure changes that are neither related to tsunamis nor seafloor coseismic displacements (the non-tsunami components) due to sensor rotation or tilt associated with ground shaking or due to long-term mechanical drift. These non-tsunami components can be a source of error when accurately estimating the tsunami source model and thus need to be removed to provide reliable coastal tsunami forecasts. This paper proposes a new method that uses time-derivative waveforms of the pressure time-series from OBP records to robustly estimate the tsunami source model, even when OBP data are perturbed by non-tsunami components. Using OBP data associated with the 2011 Off-Miyagi earthquake (M_w 7.2) and the 2016 Off-Mie earthquake (M_w 5.9), the performance of the method was evaluated when reducing artefacts due to non-tsunami components. The tsunami source model was found to be largely distorted when a conventional inversion method was used (because of the non-tsunami components). However, the artefact was dramatically reduced when using time-derivative waveforms, and the predicted coastal tsunami waveforms fitted reasonably with those of observations, thereby suggesting that the new method effectively suppresses artefacts caused by non-tsunami components. As the tsunami source models estimated from pressure and time-derivative waveforms should be similar when OBP data are not perturbed by non-tsunami components, we would be able to assess whether OBP data are perturbed by non-tsunami components by evaluating that the tsunami source models estimated from pressure waveforms and from time-derivative waveforms are similar to each other.

Key words: Tsunamis; Numerical modelling; Waveform inversion; Tsunami warning.

1 INTRODUCTION

Offshore real-time tsunami observation networks have been established over the past few decades (e.g. Kanazawa & Hasegawa 1997; Hino *et al.* 2001; González *et al.* 2005; Kaneda *et al.* 2015; Kawaguchi *et al.* 2015; Kanazawa *et al.* 2016; Uehira *et al.* 2016). A cabled tsunami observation network using ocean bottom pressure gauges (OBPs), which is known as the Dense Oceanfloor Network System for Earthquakes and Tsunamis (DONET), has been constructed off southwestern Japan by the Japan Agency for Marine-Earth Science and Technology (JAMSTEC; Fig. 1a; Kaneda *et al.* 2015; Kawaguchi *et al.* 2015). In addition, the National Research Institute for Earth Science and Disaster Resilience (NIED) has constructed an observation network, which is known as the Seafloor Observation Network for Earthquakes and Tsunamis along the Japan

Trench (S-net; Kanazawa *et al.* 2016; Uehira *et al.* 2016) off north-eastern Japan. Real-time tsunami records are often used to provide rapid and reliable tsunami forecasts (e.g. Titov *et al.* 2005; Tsushima *et al.* 2009, 2012; Baba *et al.* 2014; Gusman *et al.* 2014; Maeda *et al.* 2015; Yamamoto *et al.* 2016a, b; Tanioka 2018). For example, Tsushima *et al.* (2009, 2012) developed a tsunami forecasting algorithm (the tsunami Forecasting based on Inversion for initial Sea-surface Height; tFISH) that inverts offshore tsunami data to estimate the spatial distribution of initial sea-surface height (hereafter referred to as the tsunami source model) and then provide forecasts of coastal tsunamis based on the forward calculation.

Absolute pressure sensors manufactured by Paroscientific, Inc. (e.g. Watts & Kontoyiannis 1990; Eble & Gonzalez 1991) are commonly used for offshore tsunami observations (e.g. Kaneda *et al.* 2015; Kawaguchi *et al.* 2015; Kubota *et al.* 2015, 2017a,b;

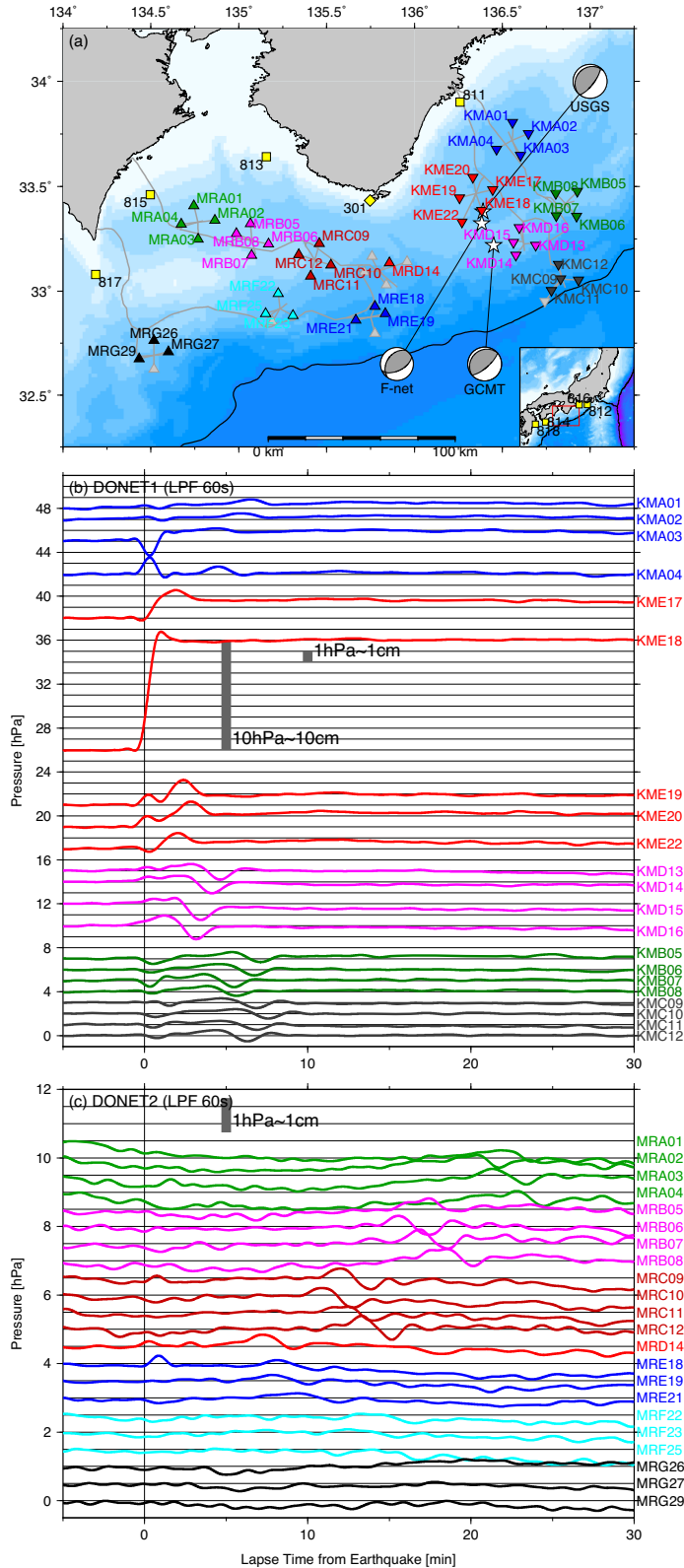


Figure 1. (a) Location map of the 2016 Off-Mie Earthquake (M_w 5.9). Stars denote centroids of CMT solutions from Global CMT (Ekstrom *et al.* 2012), F-net (Fukuyama *et al.* 1998; Kubo *et al.* 2002) and USGS. DONET1 and DONET2 OBP stations are denoted by inverted and regular triangles, respectively. OBP symbol colours denote station groups. Each OBP sensor within a group is connected to the same science node, which is a device with the function of a hub that connects the sensors to the main cable system (Kaneda *et al.* 2015; Kawaguchi *et al.* 2015). GPS buoys and coastal wave gauges are shown by yellow squares and diamonds, respectively. Pressure time-series observed by (b) DONET1 and (c) DONET2 OBPs.

Kanazawa *et al.* 2016; Uehira *et al.* 2016). However, it has been reported that the pressure outputs of the Paroscientific sensors strongly depend on their orientation relative to the Earth's gravitational field, and thus their rotation or tilting can become a source of observational errors (Chadwick *et al.* 2006). Wallace *et al.* (2016) investigated the Paroscientific OBP data of an M_w 5.9 earthquake that occurred to the southeast off Mie-Prefecture, Japan, on 2016 April 1 (hereafter referred to as the Off-Mie earthquake, Fig. 1), and suggested that an OBP observed a pressure offset increase of ~ 10 hPa nearest the epicentre (corresponding to 10 cm of subsidence; KME18 in Fig. 1a), which was related neither to the tsunami nor to coseismic seafloor displacement and was actually caused by the rotation or tilting of the sensor associated with ground shaking due to seismic waves. We here note that a pressure change of 1 hPa is equivalent to a water height change of 1 cm, if assuming a water density of 1.03 g cm^{-3} and a gravity acceleration of 9.8 m s^{-2} .

Pressure sensors manufactured by Hewlett Packard, Inc. (Karrer & Leach 1969; hereafter, HP) have also used for offshore tsunami observations (e.g. Takahashi 1981; Kanazawa & Hasegawa 1997; Hino *et al.* 2001), although they have been reported to have long-term mechanical drifts at a maximal rate of approximately 100 hPa yr^{-1} (Inazu & Hino 2011). Kubota *et al.* (2017a) investigated HP pressure data associated with a M_w 7.2 earthquake that occurred off Miyagi-Prefecture, Japan, on 2011 March 9 (hereafter referred to as the Off-Miyagi earthquake, Fig. 2) and found that the HP sensors drifted at a rate of $\sim 5 \text{ hPa hr}^{-1}$ (approximately 0.1 hPa min^{-1}) within a few hours after the occurrence of the earthquake. Long-term trends have also been found in Paroscientific sensors, with rates of less than tens of hPa yr^{-1} (e.g. Watts & Kontoyiannis 1990; Polster *et al.* 2009; Inazu & Hino 2011; Hino *et al.* 2014). Pressure offset changes and long-term trends (hereafter referred to as the non-tsunami components) neither related to tsunamis nor to seafloor permanent displacement are a large source of error when estimating tsunami source models and providing coastal tsunami forecasts.

Some studies have assessed the effects of random observation errors on tsunami forecasts (Takagawa & Tomita 2014; Tatsumi *et al.* 2014) and dynamic pressure changes associated with seismic waves (Saito & Tsushima 2016). However, it has not yet been adequately assessed how the non-tsunami components perturb the tsunami source model, and the impact of the non-tsunami components on coastal tsunami forecasts has not yet been investigated. Therefore, to provide accurate coastal tsunami forecasts, it is necessary to develop a method that reduces the perturbation (i.e. the artefacts) of the tsunami source model resulting from non-tsunami components. In this study, we thus propose such a method that uses time-derivative waveforms of the pressure time-series. We also use OBP data associated with the 2011 Off-Miyagi earthquake and the 2016 Off-Mie earthquake to assess how the conventional approach used to estimate the tsunami source model is affected when OBP data are perturbed by the non-tsunami components. Furthermore, we assess how the new method proposed in this study effectively reduces the artefacts due to non-tsunami components.

2 METHODS

The tsunami waveform inversion used to estimate the tsunami source model (hereafter referred to as the tsunami source inversion) assumes that observed waveforms can be expressed as a superposition of Green's function from small unit tsunami source elements (e.g. Baba *et al.* 2005; Tsushima *et al.* 2009; 2012; Kubota *et al.*

2015). Note that this approach does not estimate the slip distribution along the fault plane, which has been used in many previous tsunami inversion studies (e.g. Satake 1989). An observational equation for the conventional tsunami source inversion using the pressure time-series can be expressed as follows:

$$d_j^{\text{obs}}(t) = \sum_{i=1}^M G_{ij}(t) m_i, \quad (1)$$

where $d_j^{\text{obs}}(t)$ is the observed waveform at the j th station, $G_{ij}(t)$ is Green's function, which is the response to the i th unit source to the j th station (M is the total number of unit sources) and m_i is the amount of displacement of the i th unit tsunami source element. The inversion approach follows the idea that the least-square objective function, $s(\mathbf{m})$, is minimized, which is expressed as,

$$s(\mathbf{m}) = \sum_{j=1}^N \left| d_j^{\text{obs}}(t) - \sum_{i=1}^M G_{ij}(t) m_i \right|^2 \rightarrow \min, \quad (2)$$

where N denotes the total number of the stations. Eq. (1) is expressed in a vector form as

$$\mathbf{d}^{\text{obs}} = \mathbf{G}\mathbf{m}, \quad (3)$$

where \mathbf{d}^{obs} is a vector consisting of observed pressure data, \mathbf{G} is a matrix consisting of the Green's function and \mathbf{m} is a vector representing the displacement of the unit source elements. In the tsunami source inversion, a spatial smoothing constraint is often imposed as follows:

$$0 = \mathbf{S}\mathbf{m}, \quad (4)$$

where a matrix, \mathbf{S} , denotes the spatial smoothing constraints (e.g. Tsushima *et al.* 2009; Baba *et al.* 2005; Kubota *et al.* 2015). Using eqs (1) and (2), a normal equation, which is to be solved, is expressed as follows:

$$\begin{pmatrix} \mathbf{d}^{\text{obs}} \\ 0 \end{pmatrix} = \begin{pmatrix} \mathbf{G} \\ \alpha\mathbf{S} \end{pmatrix} \mathbf{m}, \quad (5)$$

where a constant α indicates the weight of the smoothing constraint. Hereafter, we refer to this approach as the conventional inversion.

When we assume that the vector \mathbf{m} (the amount of the displacement of the unit sources) does not depend on time, we can obtain the following observational equation by a temporally differentiating eq. (1) as

$$\frac{\partial d_j^{\text{obs}}}{\partial t}(t) = \sum_{i=1}^M \frac{\partial G_{ij}}{\partial t}(t) m_i, \quad (6)$$

where $\partial/\partial t$ denotes the temporal differentiation. Considering the objective function (similar to eq. 2) to be minimum, we can obtain the following equation:

$$\dot{\mathbf{d}}^{\text{obs}} = \dot{\mathbf{G}}\mathbf{m}, \quad (7)$$

where $\dot{\mathbf{d}}^{\text{obs}}$ and $\dot{\mathbf{G}}$ denote a vector consisting of the time-derivatives of the pressure data (left-hand side of eq. 6) and Green's function (right-hand side of eq. 6), respectively. A normal equation can also be expressed as

$$\begin{pmatrix} \dot{\mathbf{d}}^{\text{obs}} \\ 0 \end{pmatrix} = \begin{pmatrix} \dot{\mathbf{G}} \\ \beta\mathbf{S} \end{pmatrix} \mathbf{m}, \quad (8)$$

where β indicates the weight of the smoothing constrain (hereafter this approach is referred to as the time-derivative inversion). By solving the normal equations (eqs 5 and 8), the tsunami source model (vector \mathbf{m}) is obtained.

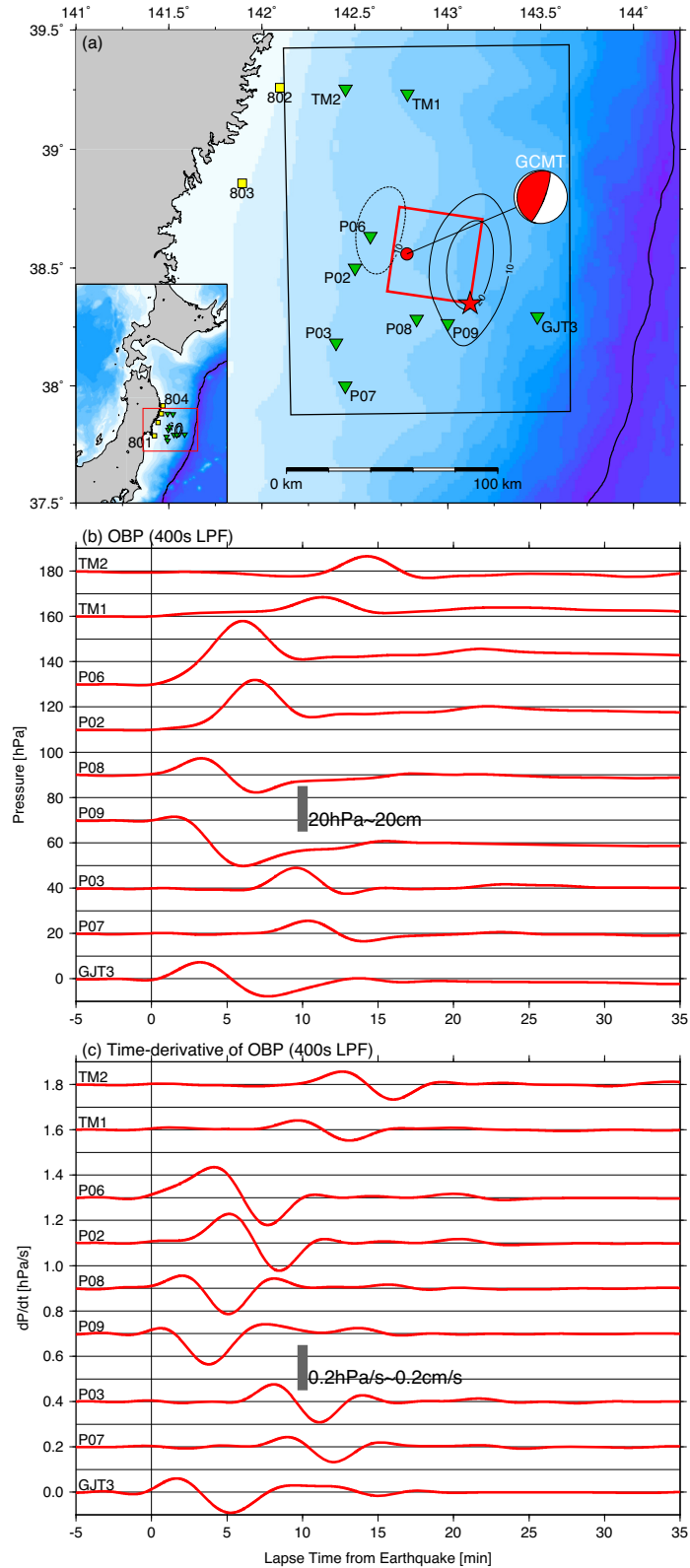


Figure 2. (a) Location map of the 2011 Off-Miyagi earthquake (M_w 7.2). Epicentre (Suzuki *et al.* 2012) and main rupture area (Kubota *et al.* 2017a) are denoted by red star and rectangle, respectively. Global CMT solution is also shown. Black contour lines are seafloor vertical displacement calculated using fault model of Kubota *et al.* (2017a); black rectangle is analysis area for tsunami source inversion; green triangles and yellow squares denote OBP stations and coastal GPS buoys, respectively. (b) Observed pressure time-series. (c) Time-derivative waveforms of OBP records.

If the pressure data (\mathbf{d}^{obs} in eq. 1) is perturbed by non-tsunami components (left-hand panel in Fig. 3), the model vector \mathbf{m} will not reflect the true tsunami source model. Approximating the pressure offset changes resulting from ground shaking as a step function (similar to OBP data at station KME18 in Fig. 1b) and the long-term trends as a linear function, the associated time-derivative waveforms would be an impulse function and a constant, respectively (right-hand panel in Fig. 3), and the time-derivative waveform of the perturbed pressure data ($\dot{\mathbf{d}}^{\text{obs}}$ in eq. 7) would be very similar to the original time-derivative waveform. However, the perturbed pressure waveform is quite different from the original pressure data, and it is thus expected that the time-derivative inversion would be less affected by non-tsunami components than conventional inversion.

3 APPLICATION TO 2011 OFF-MIYAGI EARTHQUAKE

3.1 Data and methods

We applied the time-derivative inversion to OBP data of the Off-Miyagi earthquake of 2011 March 9 (Kubota *et al.* 2017a, b) to assess the performance of the time-derivative inversion. Kubota *et al.* (2017a) estimated the finite fault model of this event (red rectangle in Fig. 2a) by inverting OBP data obtained near the focal area (green triangles in Fig. 2a). The spatial distribution of the vertical seafloor displacement calculated from the finite fault model is shown by the black contour lines in Fig. 2(a). Using the result of Kubota *et al.* (2017a) as a benchmark, we assessed the performance of the time-derivative inversion.

We used seven Paroscientific OBPs (GJT3, P02, P03, P06, P07, P08 and P09) installed by Tohoku University and two HP OBPs (TM1 and TM2) installed by the Earthquake Research Institute (ERI) of the University of Tokyo (green triangles in Fig. 2a; described in detail in Kubota *et al.* 2017a; sampling interval of 1 s). We also used data from coastal GPS buoys (Kato *et al.* 2005; Kawai *et al.* 2012) of the Port and Airport Research Institute (PARI) of the National Institute of Maritime, Port and Aviation Technology (MPAT; yellow squares in Fig. 2a) to assess the performance of the coastal tsunami forecasts.

We processed tsunami data using the following procedure, which is the same as that presented in Kubota *et al.* (2017a). We removed ocean-tide components using a theoretical tide model (Matsumoto *et al.* 2000). To reduce the high-frequency pressure changes attributed to seismic and hydroacoustic waves (e.g. Matsumoto *et al.* 2012; Saito 2013; Saito & Tsushima 2016; An *et al.* 2017, 2017; Kubota *et al.* 2017b), we then calculated the moving average with a time window of 60 s and applied a causal lowpass filter to the OBP records (a cut-off period of 400 s) and a bandpass filter to GPS buoy records (passband of 400–3600 s; Saito 1978). Furthermore, we removed hydrostatic pressure due to the water column above the OBPs, using the mean from a 20-min time window recorded prior to the focal time.

In the tsunami source inversion, we distributed 12×16 small unit source elements with a size of 20 km \times 20 km in an area of 130 km E–W \times 170 km N–S (rectangular area in Figs 4a and b) with a horizontal spacing of 10 km (overlapping with the adjacent unit sources). Details of the unit source elements are described in Kubota *et al.* (2015). For simplicity, displacement of initial sea-surface height was assumed to be equal to seafloor displacement. We calculated the tsunami Green's function using a linear long wave equation with a finite difference method in local Cartesian

coordinates (e.g. Satake 1995; Saito *et al.* 2014), and the equations used in this study were as follows:

$$\begin{aligned}\frac{\partial P}{\partial t} &= -g_0 h \frac{\partial \eta}{\partial x}, \\ \frac{\partial Q}{\partial t} &= -g_0 h \frac{\partial \eta}{\partial y}, \\ \frac{\partial \eta}{\partial t} &= -\frac{\partial P}{\partial x} - \frac{\partial Q}{\partial y},\end{aligned}\quad (8)$$

where the parameters P and Q are the vertically averaged horizontal velocity in x - and y -directions, respectively; the parameter η is the water height from the static sea surface; h is water depth and g_0 is the gravitational constant. This equation was discretized on a staggered spatial grid of 2 km by interpolating ETOPO1 1-arcmin bathymetric data (Amante & Eakins 2009). The temporal grid interval was set as 1 s. We assumed that deformation of all unit sources started simultaneously (i.e. an infinite rupture propagation velocity) and that the duration of the unit source deformation was 0 s. Static pressure offsets related to seafloor permanent deformation were considered using the method proposed by Tsushima *et al.* (2012), which subtracts the pressure change components due to seafloor deformation from the pressure change due to sea-surface fluctuation at OBP station points (a schematic illustration of this procedure is shown in Fig. S1). When calculating Green's function for the time-derivative inversion, we calculated the temporal differentiation of the calculated waveforms. Finally, we applied the same filter as those applied to observed waveforms.

In the inversion, we used a smoothing constraint weight of $\alpha = 0.5$ for the conventional inversion and $\beta = 0.01$ for the time-derivative inversion. These values were determined so that the maximal displacement of the tsunami source model would be equivalent to that of seafloor vertical deformation calculated using the finite fault model of Kubota *et al.* (2017a; black contours in Fig. 2a), which we considered to be the benchmark.

3.2 Validation of time-derivative inversion

First, to determine whether the time-derivative inversion could provide the same performance in resolving the tsunami source model as the conventional inversion, we analysed the OBP data for the Off-Miyagi earthquake. It was considered that if the OBP data had not been perturbed by non-tsunami components, then the tsunami source models estimated by both inversion methods would be similar. We used a time window from 1 to 20 min after the focal time for the inversion (white background area in Figs 4c and d). Figs 4(a) and (b) show the tsunami source models estimated using the conventional inversion and the time-derivative inversion, respectively; the results are seen to be quite similar, and both the calculated pressure and time-derivative waveforms agree well with observations (Figs 4c and d). We measured the agreement between the observed and calculated waveforms based on variance reduction (VR) as follows:

$$\text{VR} = \left(1 - \frac{\sum_i \sum_k [d_i^{\text{obs}}(k\Delta t) - d_i^{\text{calc}}(k\Delta t)]^2}{\sum_i \sum_k [d_i^{\text{obs}}(k\Delta t)]^2} \right) \times 100 (\%), \quad (9)$$

where $d_i^{\text{obs}}(k\Delta t)$ and $d_i^{\text{calc}}(k\Delta t)$ are the observed and calculated OBP data at $t = k\Delta t$ for i th OBP station, respectively (Δt is the sampling interval). We used a time window of 1 to 20 min after the focal time to calculate the VR, and obtained relatively high VRs for both pressure and time-derivative waveforms from both the conventional and time-derivative inversions (pressure waveform:

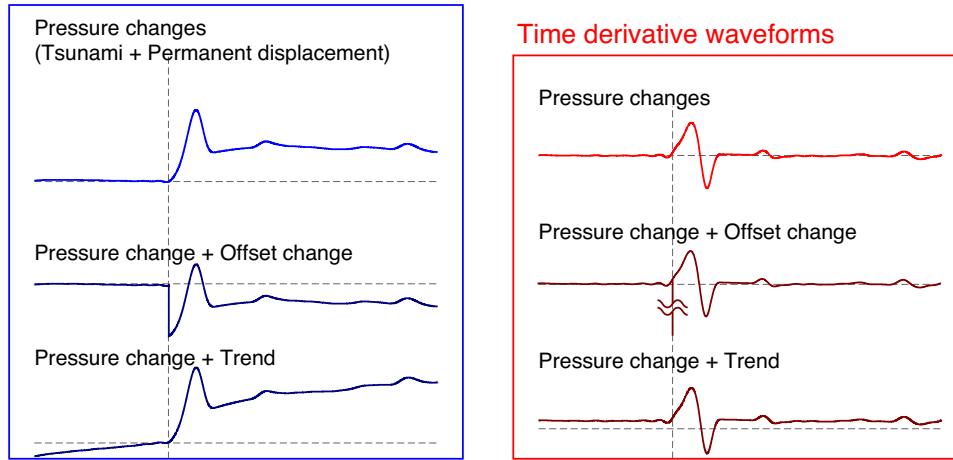


Figure 3. Schematic image of seafloor pressure change associated with earthquakes and non-tsunami components.

99.3 per cent using the conventional inversion and 96.6 per cent using the time-derivative inversion; time-derivative waveform: 97.2 per cent using the conventional inversion and 97.3 per cent using the time-derivative inversion).

Both inversion results effectively reproduce the leading tsunami waves observed by coastal GPS buoy waveforms from approximately 0–40 min (Fig. 4e). The discrepancy in the latter part of the GPS buoy waveforms (after ~40 min) is probably related to the nonlinearity and a lack of fine-scale bathymetry near the coast (e.g. Satake 1995; Saito *et al.* 2014). Figs 5(a) and (b) show comparisons of arrival times and maximal tsunami heights of the leading wave between observed and calculated tsunami waveforms (the arrival time was defined as the time when the amplitude exceeded 1 cm). The arrival times and maximal heights of the conventional inversion (blue bars in Figs 5a and b), the time-derivative inversion (red bars) and the observations (black bars) are all very close to one another. Based on these results, we thus concluded that the time-derivative inversion provided a performance as good as the conventional inversion in estimating the tsunami source model, when the OBP data are not perturbed by the non-tsunami components.

3.3 Synthetic test using data sets with non-tsunami components

We then assessed how the tsunami source model obtained using conventional inversion is perturbed by non-tsunami components (when OBP data contain non-tsunami components), and assessed how use of the time-derivative inversion reduces artefacts due to non-tsunami components. We prepared synthetic data sets by adding artificial pressure offset changes to observed OBP data from the 2011 Off-Miyagi earthquake (i.e. pressure data was artificially perturbed) and assuming pressure changes of 20–50 hPa (Fig. 6, Table 1), which correspond to those due to the rotation of Paroscientific pressure sensors with rotation angles of ~30–90° (Chadwick *et al.* 2006). We assumed the pressure offset change was a ramp function with a finite duration of $T_{\text{offset}} = 10$ s, in consideration of the duration of strong ground shaking (a few tens of seconds). The pressure offset change $p^{\text{offset}}(t)$ is expressed as follows:

$$p^{\text{offset}}(t) = \begin{cases} 0 & (t \leq 0) \\ p_o \times \frac{t}{T} & (0 < t \leq T_{\text{offset}}) \\ p_o & (T_{\text{offset}} < t) \end{cases}, \quad (10)$$

where p_o is the given pressure offset value (which is summarized in Table 1). After perturbing the pressure data, they were then processed using the same method as that applied to pressure data without the perturbation (hereafter referred to as the original data). After data processing, we considered the perturbed pressure data to be the observed data and estimated the tsunami source model. All other settings were the same as those used in the original analysis described in the previous section. Note that the first 1-min of data were not used for the inversion because of the instability of the pressure data.

The inversion results are shown in Fig. 6, where it is evident that the estimation of the tsunami source model with the conventional inversion (Fig. 6a) is quite different from that estimated using original data (Fig. 4). The pressure waveforms calculated from the tsunami source model obtained by the conventional inversion (blue lines in Fig. 6c) explain the artificially-perturbed (i.e. observed) pressure waveforms (grey dashed lines in Fig. 6c) very well (VR = 99 per cent), but the original pressure waveforms (black lines) are not explained at all (VR = –1466 per cent). However, the time-derivative calculated pressure waveforms from the tsunami source model (blue lines in Fig. 6d) do not explain the initial part (<~5 min) of the time-derivative waveforms relating to original pressure waveforms, but the latter part is reasonably explained (VR = –142 per cent). Although the tsunami source model obtained using the time-derivative inversion (Fig. 6b) is similar to that obtained by original data, the results are not exactly the same. The pressure waveforms calculated from this tsunami source model explain the original pressure waveforms reasonably well (red lines in Fig. 6c, VR = 44.9 per cent), and the discrepancy found between the time-derivative waveforms of observational and synthetic data is much smaller than that for the conventional inversion (red lines in Fig. 6d, VR = 80.1 per cent). These results show that the conventional inversion is unable to remove the artefacts due to pressure offset changes, whereas the time-derivative inversion dramatically reduces them.

Although the artefact is dramatically reduced by the time-derivative inversion, artefacts due to the offset changes are not completely removed; this is considered likely to be related to the temporal smoothing effect due to the moving average and the low-pass filter (grey dashed lines in Fig. 6d). However, we find that the forecasted arrival time and maximal amplitude at the coastal GPS buoys (blue bars in Figs 5c and d) tend to be early and large (by ~5–10 min and ~5 cm, respectively) compared to observations (black bars) when conventional inversion is used, but they are reasonably

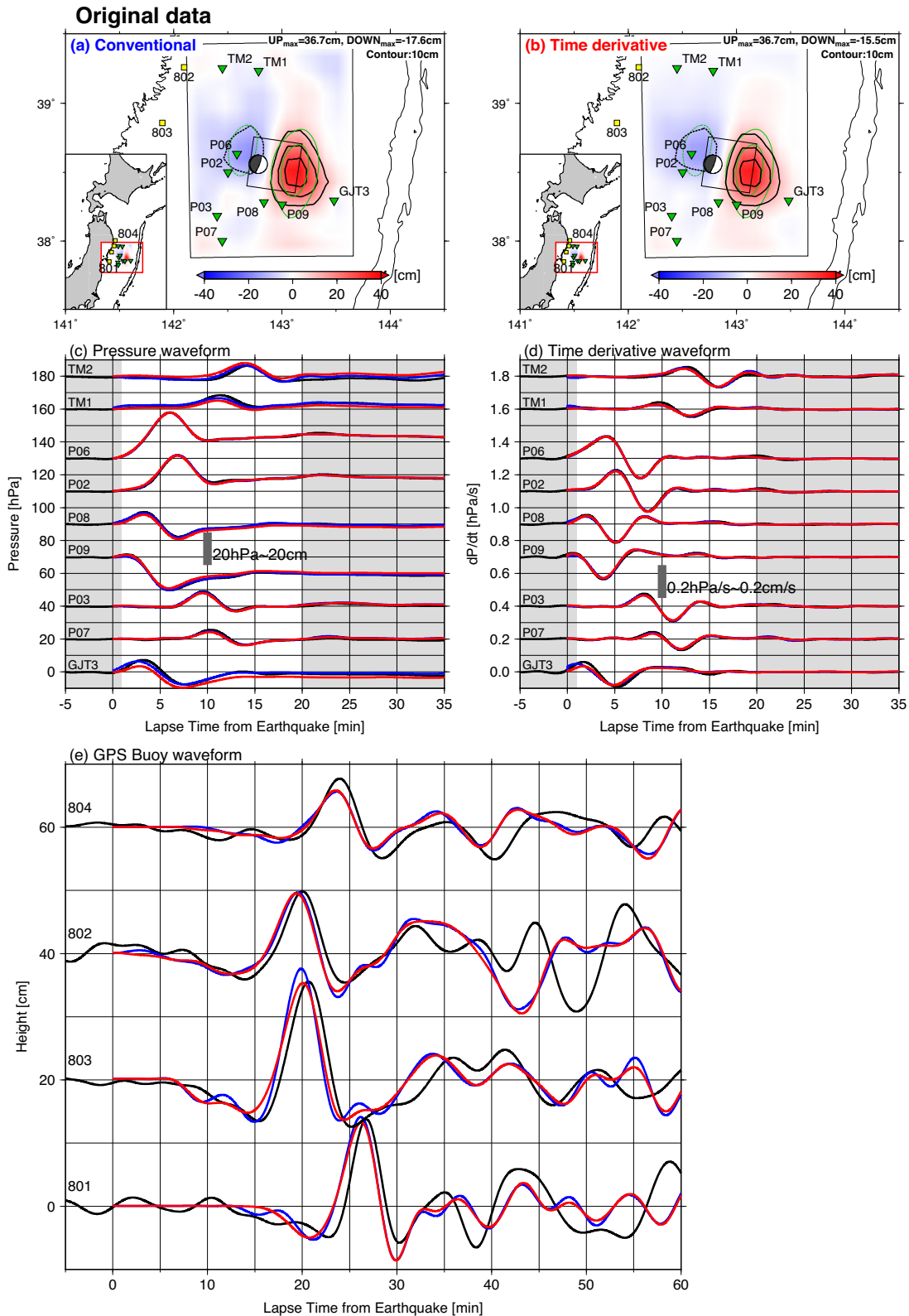


Figure 4. Inversion results for the 2011 Off-Miyagi earthquake using OBP data without adding artificial perturbation (original data). Tsunami source models obtained using (a) conventional inversion and (b) time-derivative inversion. Uplifted and subsided areas are shown in red and blue, respectively; green contour lines are the seafloor vertical displacement expected using the fault model of Kubota *et al.* (2017a) with 10-cm intervals. Comparisons of (c) pressure and (d) time-derivative waveforms between observed waveforms (black) and calculated waveforms. Waveforms calculated from source models obtained using conventional and time-derivative inversions are shown in blue and red, respectively. A time window from 1 to 20 min (white background area) was used in the inversion. (e) Comparison of coastal GPS buoy waveforms between observed (black) and forecast (blue and red) waveforms.

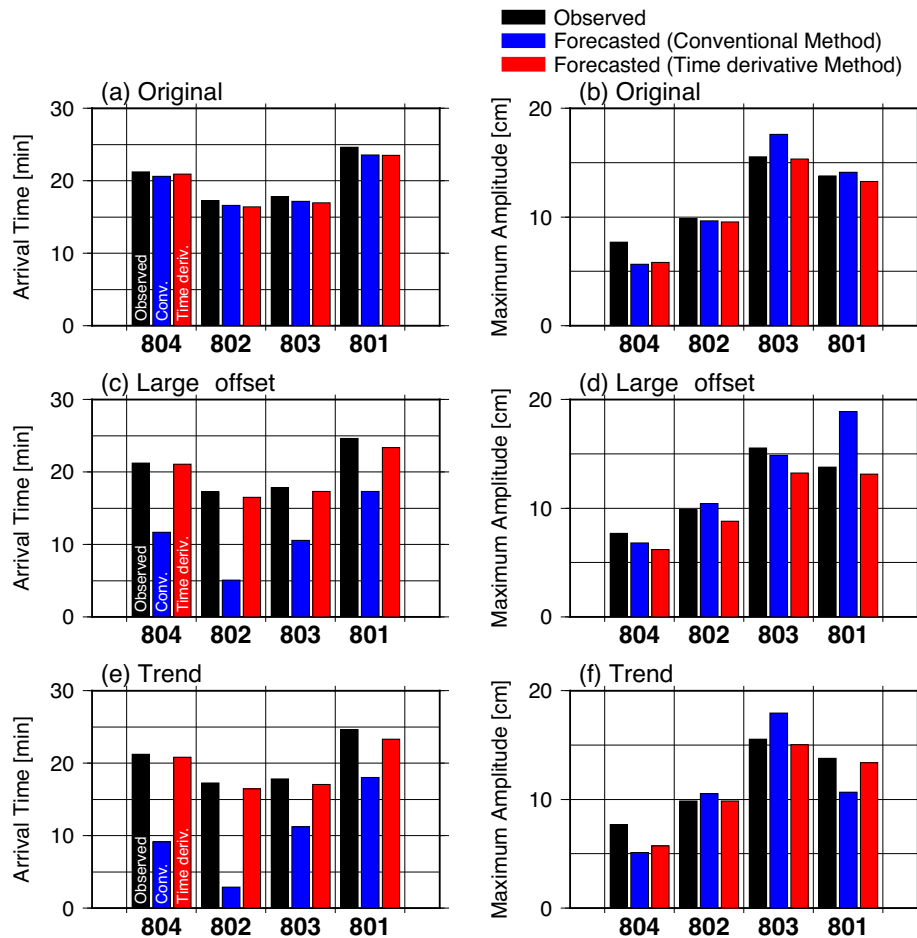


Figure 5. Comparison of arrival times of first waves and maximal amplitudes between observation (black) and forecasts from conventional inversion (blue) and time-derivative inversion (red), using (a, b) original pressure data (Fig. 4), (c, d) synthetic pressure data with pressure offset changes (Fig. 6) and (e, f) synthetic pressure data with a long-term trend (Fig. S2).

explained when the time-derivative inversion is used (red bars in Figs 5c and d).

We also conducted tests assuming a linear pressure trend at a rate of 0.5 hPa min^{-1} (Fig. S2) and smaller pressure offset values (less than 10 hPa; Figs S3 and S4). All results show that artefacts due to non-tsunami components are reduced well using the time-derivative inversion; however, these results are not achieved when using the conventional inversion. The forecast tsunami arrival time and maximal height of the GPS buoys using the synthetic data set containing linear trends (Fig. S2) are shown in Figs 5(e) and (f), respectively. When using the conventional inversion, the forecast arrival time is approximately 10 min earlier than the observation, whereas it is nearly similar to the observation when the time-derivative inversion is used. These synthetic tests thus demonstrate that the time-derivative inversion effectively reduces the artefacts in the tsunami source model due to the non-tsunami components and improves the forecast of the arrival time and maximal height of the coastal tsunami.

4 APPLICATION TO 2016 OFF-MIE EARTHQUAKE

4.1 Data and analysis

In this section, we report results of applying the time-derivative inversion to OBP data from the M_w 5.9 Off-Mie earthquake (Wallace *et al.* 2016; Asano 2018; Nakano *et al.* 2018; Takemura *et al.* 2018). The pressure changes due to the tsunami with a maximal amplitude of $\sim 2 \text{ hPa}$ (equivalent to a tsunami of $\sim 2 \text{ cm}$) were clearly observed by the DONET OBPs, and a few hPa of pressure offset-level changes were also observed at DONET1 stations near the epicentre (for example, KME17, KM19, KME20 and KME22; Fig. 1b). One OBP station nearest the epicentre (KME18) observed a large pressure offset change of approximately 10 hPa, which could be attributed to the tilting or rotation of the sensors in relation to strong ground shaking, as noted by Wallace *et al.* (2016). Kubo *et al.* (2018), investigated the site amplification characteristics of DONET1 stations and found that station groups KMA and KME (blue and red inverted triangles in Fig. 1a) had large site amplifications due to thick subseafloor sediments. Kubo *et al.* (2018) and Nakamura *et al.* (2018) reported peak ground accelerations (PGAs) of $\sim 700 \text{ gal}$ by DONET strong motion seismometers at KME18 during the 2016 Off-Mie earthquake, and also found that the site amplification observed at KME18 during this event was more than

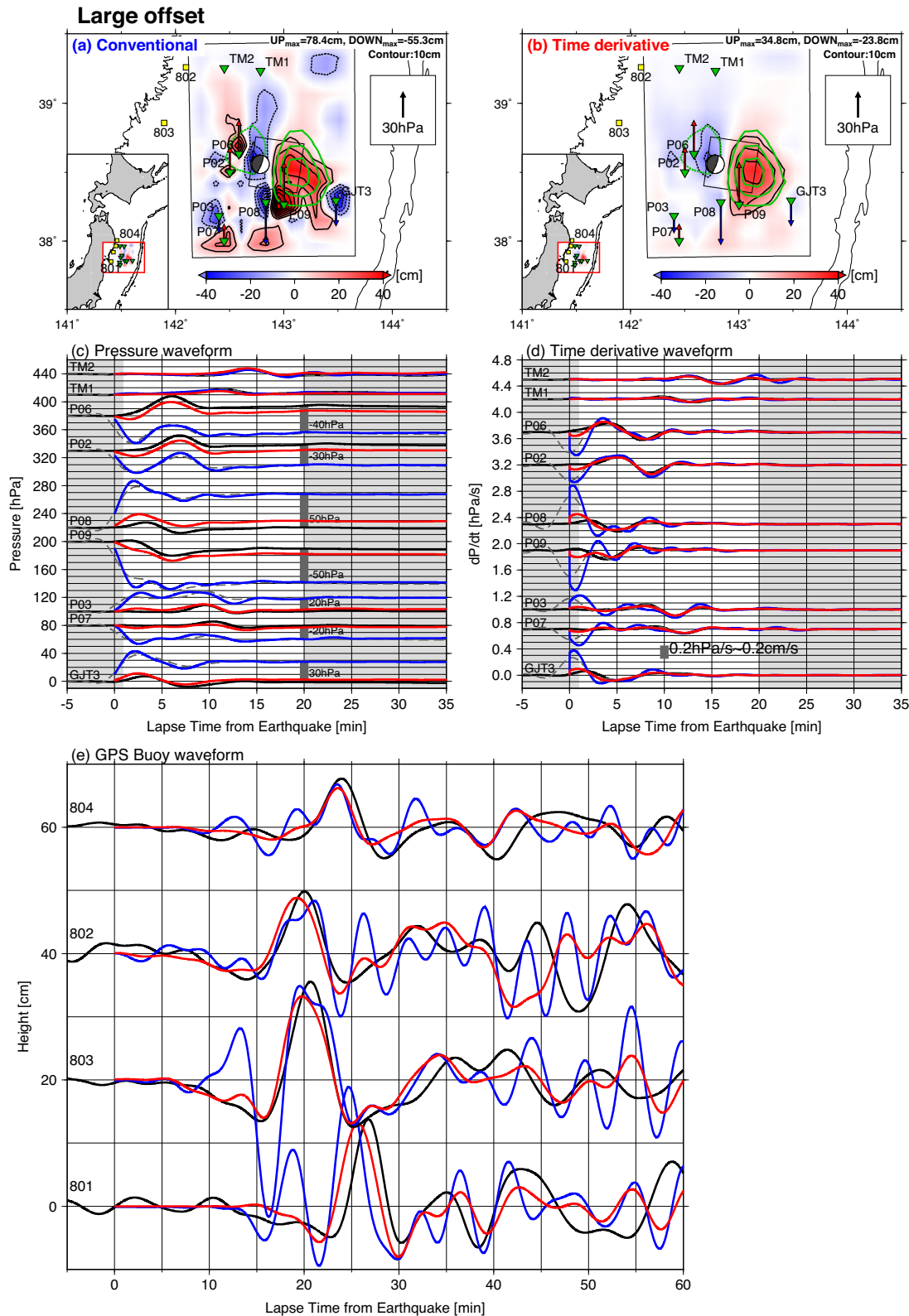


Figure 6. Inversion results of the 2011 Off-Miyagi earthquake using synthetic OBP data containing artificial pressure offset changes. Tsunami source model from OBP data without artificial perturbation using conventional inversion (Fig. 4a) shown by green contours; grey dashed lines in (c) and (d) are synthetic data used in analysis; other explanations are same as those in Fig. 4.

40 times larger than that expected from the empirical relation. In addition, Kubo *et al.* (2018) suggested that a non-linear soil response

occurred at DONET1 seismometers near the epicentre. These results support the idea that the pressure waveform at KME18 station is

Table 1. Perturbations to OBP data in synthetic test.

Case Unit	Original hPa Fig. 4	Large offset hPa Fig. 6	Trend hPa min ⁻¹ Fig. S2	Small offset hPa Fig. S3	Offset at P06 hPa Fig. S4
GJT3	0	+30	+0.5	+10	0
P02	0	-30	+0.5	+5	0
P03	0	+20	+0.5	+5	0
P06	0	-40	-0.5	+5	-30
P07	0	-20	-0.5	+5	0
P08	0	+50	-0.5	+10	0
P09	0	-50	-0.5	+15	0
TM1	0	0	+0.5	0	0
TM2	0	0	-0.5	0	0

perturbed by non-tsunami components due to strong ground shaking. Therefore, when estimating the tsunami source model, data from the OBP at station KME18 were excluded.

We processed DONET OBP data using the same method as used with the 2011 Off-Miyagi earthquake (cut-off period of the low-pass filter was 60 s). We estimated the tsunami source model (Fig. 7) by manually selecting OBP stations and time windows used for inversion based on a visual inspection of OBP waveforms (drawn by thick black lines in Fig. S6). As it was suspected that DONET1 OBP waveforms at stations near the epicentre were also perturbed by non-tsunami components (as with station KME18), due to the large peak ground acceleration during the earthquake (Kubo *et al.* 2018; Nakamura *et al.* 2018), OBP data from stations KMA03, KMD15, KMD16, KME17, KME19, KME20 and KME22 were also excluded (in addition to KME18) from analysis (grey inverted triangles in Fig. 7). Furthermore, coastal tsunami data were not used to discuss the accuracy of the coastal tsunami forecast, because the observed tsunami height at the coast was very small (less than a few cm). We set the analytical area as 100 km × 100 km. To avoid both overfitting and oversmoothing during analysis, we used smoothing constraint weights of $\alpha = 0.5$ for the conventional inversion and $\beta = 0.01$ for the time-derivative inversion, which were determined based on the trade-off curve between the smoothing weight and the VR values (Fig. S5).

4.2 Results

The estimated tsunami source models obtained from conventional and time-derivative inversions were found to be similar to each other (Figs 7a and b, respectively), and a pair of uplift and subsidence areas with maximal amplitudes of approximately +3 and -2 cm, respectively, were estimated. To compare the tsunami source model with the seismic analysis, we calculated the seafloor vertical displacement based on the centroid moment tensor (CMT) solution of the U.S. Geological Survey (USGS). In this calculation, we assumed one planar rectangular fault such that its centre coincided with the USGS centroid. The fault length, width, and slip amount were assumed using the scaling law of Wells & Coppersmith (1994), and vertical displacement was calculated using the equations of Okada (1992). We obtained a maximal seafloor vertical deformation displacement of approximately 3 cm (green contours in Fig. 7), which is consistent with that of the tsunami source model. The vertical displacement of the tsunami source model at OBP station KME18 was approximately +1 cm, which is much smaller than that expected from the observed pressure change (~-10 cm). This indicates that the large offset pressure change at station KME18 was neither due to the tsunami nor to seafloor permanent displacement, but due to

non-tsunami components. The strike of the hinge-line between the uplift and subsidence is consistent with the strike angle of the finite fault model of Wallace *et al.* (2016; 215°, yellow rectangles in Figs 7a and b). The vertical displacements expected from our tsunami source model at stations KMA03, KME17 and KME22 are less than 1 cm (Fig. S6a) and are therefore inconsistent with the observed pressure changes (displacements of approximately 1 cm). However, the arrival times, amplitudes and durations of the tsunami are reasonably consistent with those of the observation. In addition, the expected coastal tsunami heights of the conventional and time-derivative inversions are similar (e.g. approximately 1.5 cm at station 301) (Fig. S6e).

To investigate the discrepancies of pressure offset changes at stations KMA03, KME17 and KME22 between calculations and observations, we conducted an inversion that included OBP data obtained near the epicentre (KME18 was excluded from analysis) (Figs S7 and S8) and compared the result with the tsunami source model excluding the stations near the epicentre (Fig. 7, hereafter referred to as the reference tsunami source model). We found that the tsunami source model obtained using the time-derivative inversion (Fig. S7b) was similar to the reference tsunami source model, whereas the tsunami source model using the conventional inversion had a wider subsidence area extending around stations KMA03, KME17 and KME22 (Fig. S7a). Since the tsunami source models using the conventional and time-derivative inversions should resemble one another when OBP data are not perturbed by non-tsunami components (as shown in the previous section), the discrepancy of the tsunami source models suggests that OBP data from stations KMA03, KME17 and KME22 are also perturbed by non-tsunami components, although the amplitudes are very small (approximately 1 cm).

Tsuji *et al.* (2017) interpreted the rupture process of this earthquake as being related to an ancient splay fault system in an accretionary prism (Tsuji *et al.* 2014), based on the comparison of the strike angles between of the ancient splay fault and of the finite fault model of Wallace *et al.* (2016) (yellow rectangle in Fig. 7). However, as the tsunami source model estimated using the conventional inversion strongly depends on non-tsunami components, it is difficult to discuss the rupture process of the Off-Mie earthquake, as previously discussed by Tsuji *et al.* (2014), whereas we can discuss it by using the time-derivative inversion, which can reduce the artefacts of the tsunami source model. In addition, conducting a comparison between tsunami source models from both inversions is effective for distinguishing whether or not near-source OBPs contain the non-tsunami component. The time-derivative inversion is thus useful for discussing the detailed rupture processes of tsunami-associated

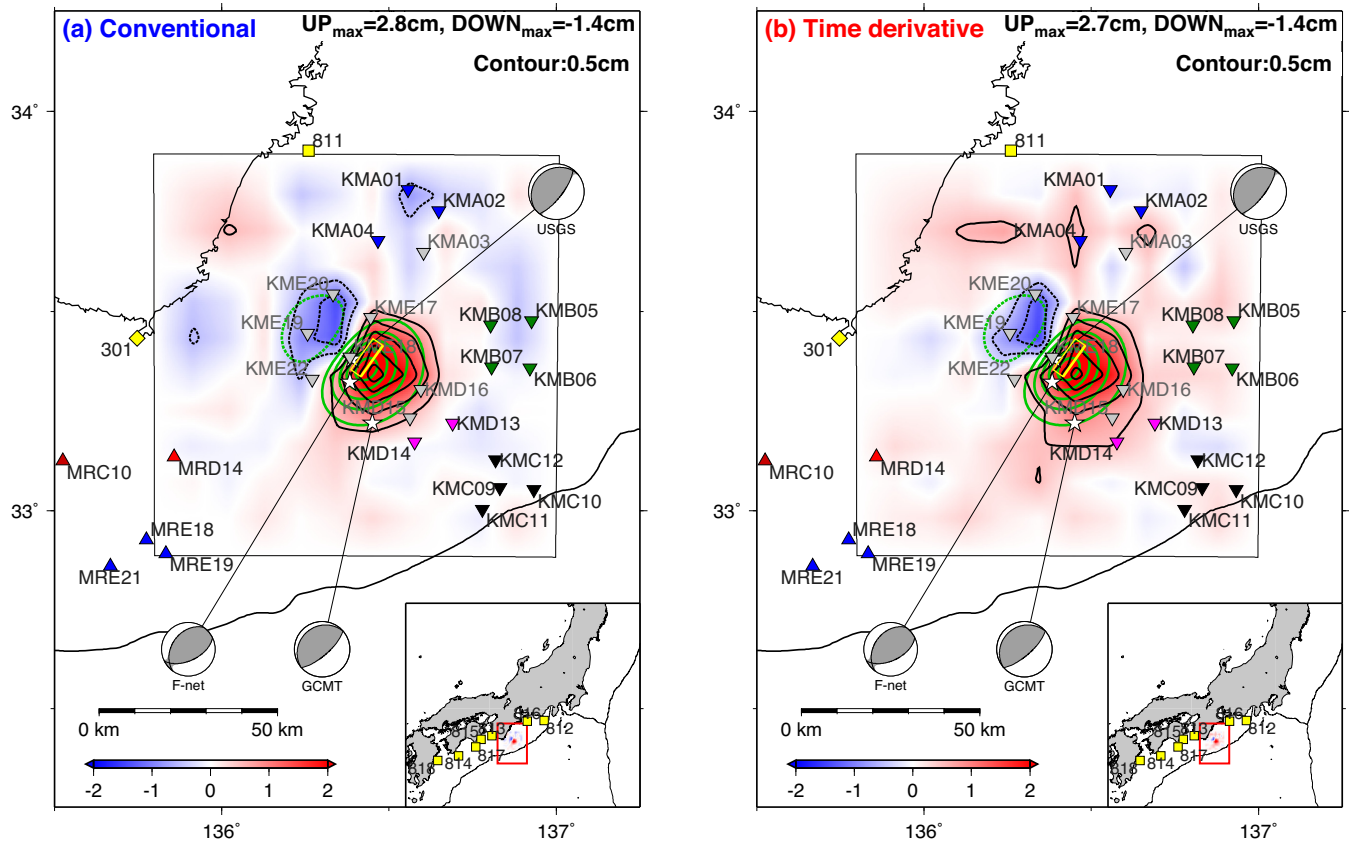


Figure 7. Tsunami source model of the 2016 Off-Mie earthquake obtained using (a) conventional and (b) time-derivative inversions, without OBP data near the epicentre (OBPs not used in analysis are shown in grey). Colours of OBPs used in the inversion are the same as Fig. 1. The interval of the contour lines is 0.5 cm. Green contours denote seafloor vertical displacement expected from the USGS CMT solution; yellow rectangles denote finite fault model of Wallace et al. (2016).

earthquakes, which is not easily achieved using the conventional inversion alone.

For a real-time tsunami forecast, we conducted a tsunami source inversion using only the early part of DONET OBP data (a time window from 1 to 5 min following the focal time) (Fig. 8). As there was no time to inspect OBP data to exclude waveforms containing non-tsunami components from the tsunami source inversion, we also used OBP data from station KME18, which contained a large apparent pressure offset change. When using the conventional inversion, a large amount of subsidence (approximately -10 cm) was estimated around station KME18 (Fig. 8a) and results from the tsunami source model were found to be quite different from those of the reference tsunami source model (Fig. 7). However, results from the tsunami source model using the time-derivative inversion (Fig. 8b) were very similar to those of the reference tsunami source model, which suggests that the time-derivative inversion effectively reduces non-tsunami components, even when providing a real-time analysis. The latter part of OBP waveforms calculated from the tsunami source model obtained by conventional inversion (blue lines in Fig. S8) do not match the observations at all, whereas that using the time-derivative inversion provide a reasonable fit (red lines in Fig. S9). Although the expected coastal tsunami height is only a few centimetres, which is less than the noise level (Fig. S9e), the expected maximal amplitudes at coastal stations using the conventional inversion (blue lines in Fig. S9e) are nearly twice as large as the forecast using the time-derivative inversion (red lines).

5 DISCUSSION

To provide an accurate and reliable tsunami forecast, it is important to quickly obtain highly accurate information from the tsunami source model. We thus investigated the relationship between the tsunami source inversion and the end time of the inversion time window using OBP data associated with the 2011 Off-Miyagi earthquake (Fig. 9). Changing the end time of the inversion time window from 2 to 20 min after the focal time (the start time of the time window was fixed to 1 min), we conducted a tsunami source inversion. The other settings were the same as those of the original analysis.

To evaluate the temporal stability of the inversion, we investigated the temporal evolution of the VR for the observed and calculated waveforms using a time window of 1–20 min (Fig. 9a). We also calculated the temporal evolution of the total volume of displaced seawater (V) (Fig. 9b), which is defined as follows:

$$V = \sum_i \sum_j |u_{ij}| \times \Delta x \times \Delta y, \quad (11)$$

where u_{ij} is the displacement of the tsunami source at the (i, j) th grid in the x and y directions (Δx and Δy are the horizontal grid intervals of 2 km). The temporal evolution of the VR for pressure waveforms and total volumes was found to be quite similar for the two inversion methods; however, the temporal evolution of the total volume was stable after 10 min when the time-derivative inversion was used (Fig. 9b). These results suggest that the time-derivative inversion is not necessarily better than the conventional inversion

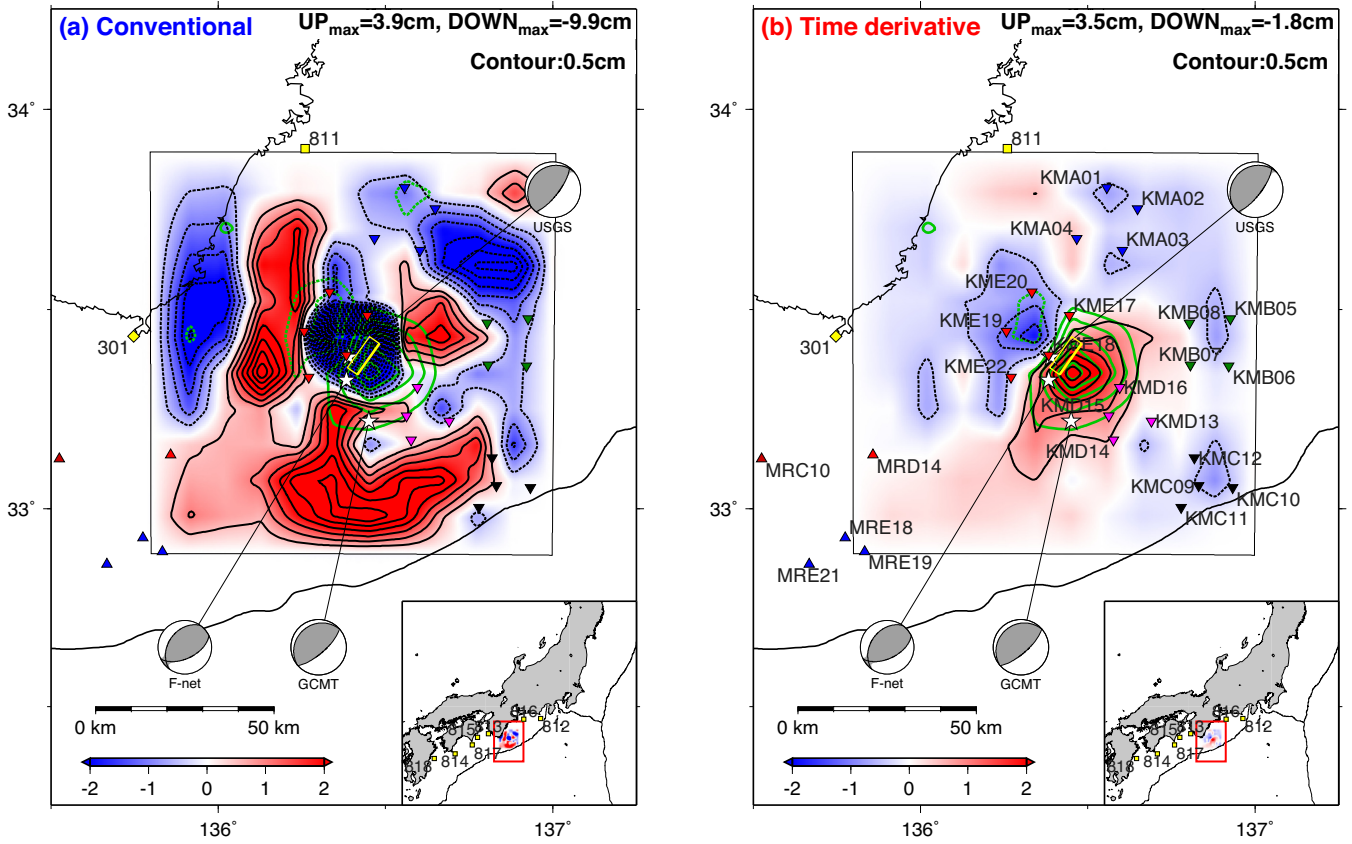


Figure 8. Tsunami source model of the 2016 Off-Mie earthquake obtained using (a) conventional and (b) time-derivative inversions with all the OBPs and a time window of 1–5 min. Green contours denote seafloor vertical displacement obtained in post-analysis (Fig. 7a); other explanations are same as those in Fig. 7.

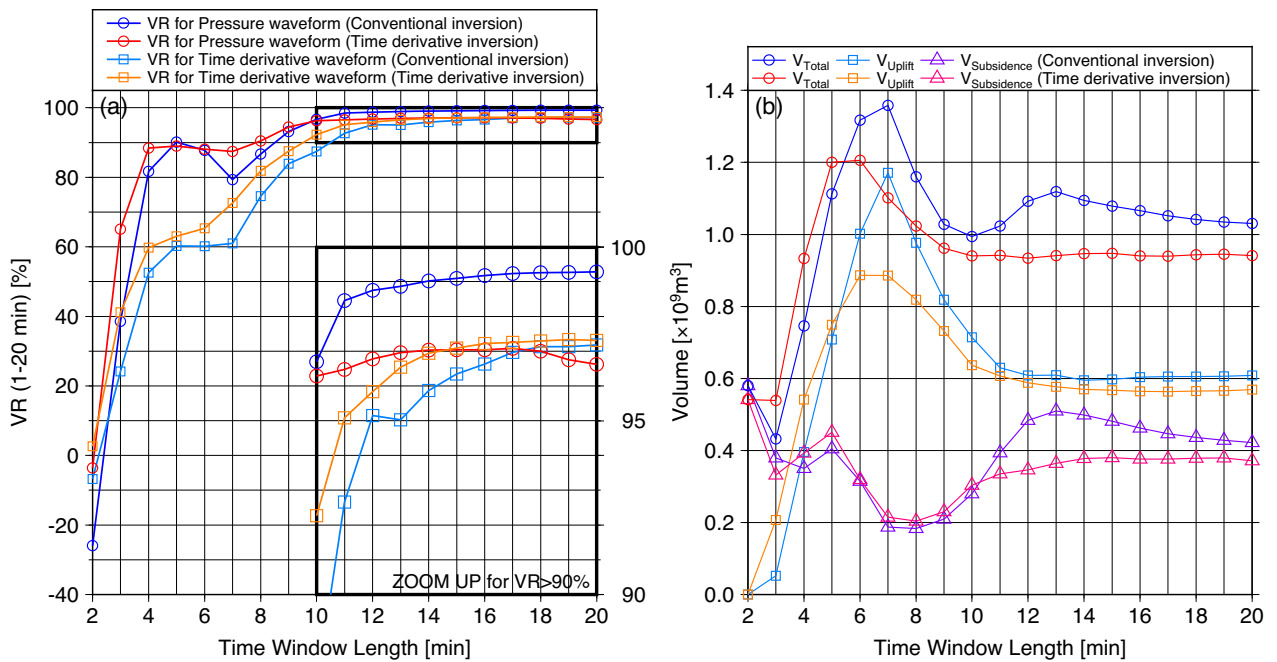


Figure 9. (a) Temporal evolution of VR between observed and calculated waveforms using time window from 1 to 20 min. VR of pressure waveform obtained using conventional (blue) and time-derivative (red) inversions, and time-derivative waveform obtained using conventional (light blue) and time-derivative (red) inversions. (b) Temporal evolution of volumes of displaced seawater. Temporal evolution of total displacement (blue and red), uplifted region (light blue and orange) and subsided region (purple and pink) are shown.

with respect to convergence time, but it is slightly better in terms of stability.

There would be another approach to simultaneously estimate the tsunami source model and the non-tsunami component at each OBP station from pressure waveforms. The advantage of such approach would be that the first few minutes of data following the occurrence of the earthquake could be used to estimate the tsunami source model, although our approach did not use. However, such an approach should have a trade-off between the estimated seafloor displacement and the estimated non-tsunami components (an example of this possible trade-off is shown in Fig. S10). If a shorter time window were used that did not include the peak amplitude of the tsunami, it would be possible that the gradual pressure change associated with the tsunami is wrongly estimated as a linear trend. This would be a disadvantage to provide fast ($< \sim 10$ min from the earthquake) and reliable tsunami forecasts. Our approach using time-derivative waveforms is advantageous in avoiding such trade-off, because only the displacement of the unit tsunami source elements are the unknown parameters.

In a practical tsunami forecast, we also need to consider the artefacts due to high-frequency pressure changes associated with seismic and hydroacoustic waves (e.g. Matsumoto *et al.* 2012; Saito 2013; An *et al.* 2017, 2017; Kubota *et al.* 2017b); although these effects are not included in the analysis. As the dominant period of hydroacoustic waves is less than ~ 10 s (e.g. Matsumoto *et al.* 2012; Saito 2013, 2017), whereas tsunami waves have much longer dominant periods ($> \sim 100$ s), hydroacoustic components can be removed from OBP waveforms by applying a lowpass filter with an appropriate cut-off period. In addition, previous studies have also reported dynamic pressure changes caused by the reaction force from the seawater to the seafloor (in response to the seafloor accelerating the seawater during seafloor displacement) (a dominant period of $< \sim 50$ s), (e.g. An *et al.* 2017; Saito 2017; Kubota *et al.* 2017b). However, although it appears that this component may affect the inversion, Saito & Tsushima (2016) found that the effects are only minimal, because such short-period pressure components cannot be expressed by the superposition of Green's function of the tsunami [which has much longer dominant periods ($> \sim 100$ s)]. We also note that in the practical tsunami forecast the consideration of the additional time to process OBP data is required. But it would not be a major concern with respect to the proficiency of contemporary hardware, and will be even less of a concern when using high-performance computers developed in the future.

In the investigation of the temporal evolution of inversion stability, we used OBP data that were not perturbed by non-tsunami components. Our results showed similar temporal evolutions for both the conventional and time-derivative inversions. In the synthetic test we assumed that the pressure data were perturbed by non-tsunami components and found that the tsunami source models for conventional and time-derivative inversions were very different. Based on these results, it would be very useful to compare tsunami source models using conventional and the time-derivative inversions to enable a real-time validation of pressure data quality and to distinguish whether or not pressure data contain non-tsunami components in real time.

6 CONCLUSIONS

We propose a new method using the time-derivative waveforms of the pressure time-series (rather than the raw pressure time-series) to estimate the spatial distribution of initial sea-surface height (the

tsunami source model) using OBP data, with the aim of reducing artefacts due to non-tsunami pressure components. Using OBP data associated with the Off-Miyagi earthquake that occurred on 2011 March 9 (M_w 7.2), the proposed method was found to work as well as the conventional method. We also conducted a performance test using a synthetic data set and artificially perturbing OBP data. The tsunami source model obtained using the conventional inversion approach provided large seafloor displacements around OBPs due to artificial non-tsunami components, and the forecast coastal tsunami arrived earlier and had a larger amplitude than the observation. However, when time-derivative waveforms were used for the inversion, artefacts due to non-tsunami components were dramatically suppressed, and the forecast coastal tsunami waveforms reasonably matched those of the observation.

We also applied the new method to OBP data associated with the 2016 Off-Mie earthquake (M_w 5.9), and the estimated tsunami source model was found to be consistent with the USGS CMT solution. The tsunami source model also suggested that OBPs near the epicentre contained non-tsunami components (with an amplitude of approximately 1-cm) because of sensor tilting or rotation. We then analysed OBP data based on quasi-real-time analysis, and the estimated tsunami source model obtained using the conventional method provided very different results from those obtained using post-analysis. However, the newly developed tsunami source model provided results that were quite similar to those obtained by careful post-analysis, even when including OBP data perturbed by non-tsunami components.

We assessed the time window used for inversion to discuss the temporal stability of the inversion and found that the tsunami source model obtained using the time-derivative inversion was stable after inversion convergence (~ 10 min from the focal time), whereas the total volume of displaced seawater was unstable when the conventional method was used. For practical tsunami forecasting, it would be useful to compare tsunami source models using both inversion methods to validate real-time OBP data quality, as it is considered that the methods would provide identical results if OBP data are not perturbed by non-tsunami components and the results will be different if OBP data are perturbed.

ACKNOWLEDGEMENTS

The authors thank Editor Frederik Simons and Reviewers Eric Geist and Sebastien Allgeyer for their useful and helpful comments, which improved the manuscript. This study was supported by the Council for Science, Technology and Innovation (CSTI) through the Cross-Ministerial Strategic Innovation Promotion Program (SIP) entitled 'Enhancement of societal resiliency against natural disasters'. This study was also supported by Japan Society for the Promotion of Science (JSPS) KAKENHI Grant Numbers JP20244070 and JP26000002 and the research project 'Research concerning Interaction between the Tokai, Tonankai, and Nankai Earthquakes' of the Ministry of Education, Culture, Sports, Science and Technology (MEXT), Japan. The authors would like to thank Tatsuhiko Saito, Hiroaki Tsushima, Shunsuke Takemura, and Hisahiko Kubo for the fruitful discussions. The authors would further like to thank the ERI and PARI for providing tsunami data, and Global CMT, USGS and F-net for the CMT solution data. OBP data of the 2011 Off-Miyagi earthquake installed by Tohoku University is available by contacting T. Kubota. DONET was developed by JAMSTEC (http://www.jamstec.go.jp/ceat/donet_data/e/) and is being jointly operated by NIED and JAMSTEC from 2016 April 1. The repository

web site of DONET data is now under construction and will be available soon. The figures in this paper were prepared using Generic Mapping Tools (GMT) (Wessel & Smith 1998). The authors used the English language editing service Editage (www.editage.jp).

REFERENCES

- Amante, C. & Eakins, B.W., 2009. ETOPO1 1 arc-minute global relief model: Procedures, data sources and analysis, in *NOAA Tech. Memo. NESDIS NGDC-24*, pp. 19, Natl. Geophys. Data Center, NOAA, Boulder, CO, doi:10.7289/V5C8276M.
- An, C., Cai, C., Zheng, Y., Meng, L. & Liu, P., 2017. Theoretical solution and applications of ocean bottom pressure induced by seismic seafloor motion, *Geophys. Res. Lett.*, **44**, 10 272–10 281.
- Asano, K., 2018. Source Modeling of an Mw 5.9 Earthquake in the Nankai trough, southwest Japan, using offshore and onshore Strong-Motion waveform records, *Bull. seism. Soc. Am.*, **108**, 1231–1239.
- Baba, T., Cummins, P.R. & Hori, T., 2005. Compound fault rupture during the 2004 off the Kii Peninsula earthquake (M 7.4) inferred from highly resolved coseismic sea-surface deformation, *Earth Planets Space*, **57**, 167–172.
- Baba, T., Takahashi, N. & Kaneda, Y., 2014. Near-field tsunami amplification factors in the Kii Peninsula, Japan for Dense Oceanfloor Network for Earthquakes and Tsunamis (DONET), *Mar. Geophys. Res.*, **35**, 319–325.
- Chadwick, W.W., Jr., Nooner, S.L., Zumberge, M.A., Embley, R.W. & Fox, C.G., 2006. Vertical deformation monitoring at Axial Seamount since its 1998 eruption using deep-sea pressure sensors, *J. Volc. Geotherm. Res.*, **150**, 313–327.
- Eble, M.C. & Gonzalez, F.I., 1991. Deep-ocean bottom pressure measurements in the Northeast Pacific, *J. Atmos. Oceanic Technol.*, **8**, 221–233, doi:10.1175/1520-0426(1991)008<0221:DOBPMI>2.0.CO;2.
- Ekstrom, G., Nettles, M. & Dziewonski, A.M., 2012. The global CMT project 2004–2010: centroid-moment tensors for 13,017 earthquakes, *Phys. Earth planet. Inter.*, **200–201**, 1–9.
- Fukuyama, E., Ishida, S., Dreger, D.S. & Kawai, H., 1998. Automated seismic moment tensor determination by using on-line broadband seismic waveforms, *J. seism. Soc. Jpn. 2nd Ser.*, **51**, 149–156. (in Japanese with English abstract), doi:10.4294/zisin1948.51.1.149.
- González, F.I., Bernard, E.N., Meinig, C., Eble, M.C., Mofjeld, H.O. & Stalin, S., 2005. The NTHMP tsunameter network, *Nat. Hazards*, **35**, 25–39.
- Gusman, A.R., Tanioka, Y., Macinnes, B.T. & Tsushima, H., 2014. A methodology for near-field tsunami inundation forecasting: application to the 2011 Tohoku tsunami, *J. geophys. Res.: Solid Earth*, **119**, 8186–8206.
- Hino, R., Tanioka, Y., Kanazawa, T., Sakai, S., Nishino, M. & Suyehiro, K., 2001. Micro-tsunami from a local interplate earthquake detected by cabled offshore tsunami observation in northeast Japan, *Geophys. Res. Lett.*, **28**, 3533–3536.
- Hino, R. *et al.*, 2014. Was the 2011 Tohoku-Oki earthquake preceded by aseismic preslip? Examination of seafloor vertical deformation data near the epicenter, *Mar. Geophys. Res.*, **35**, 181–190.
- Inazu, D. & Hino, R., 2011. Temperature correction and usefulness of ocean bottom pressure data from cabled seafloor observatories around Japan for analyses of tsunamis, ocean tides, and low-frequency geophysical phenomena, *Earth Planets Space*, **63**, 1133–1149.
- Kanazawa, T. & Hasegawa, A., 1997. Ocean-bottom observatory for earthquakes and tsunami off Sanriku, north-east Japan using submarine cable, in *Presented at International Workshop on Scientific Use of Submarine Cables*, Okinawa, Japan.
- Kanazawa, T. *et al.*, 2016. S-net project, cabled observation network for earthquakes and tsunamis, in *Abstract WE2B–3, Presented at SubOptic 2016*, Dubai, April 18–21.
- Kaneda, Y. *et al.*, 2015. Development and application of an advanced ocean floor network system for megathrust earthquakes and tsunamis, in *Seafloor Observatories*, pp. 643–662, eds Favali, P. *et al.*, Springer, doi:10.1007/978-3-642-11374-1_25.
- Karrer, H.E. & Leach, J., 1969. A quartz resonator pressure transducer, *IEEE Trans. Ind. Electron. Control Instrum.*, **16**, 44–50.
- Kato, T., Terada, Y., Ito, K., Hattori, R., Abe, T., Miyake, T., Koshimura, S. & Nagai, T., 2005. Tsunami due to the 5 September 2004 off the Kii Peninsula Earthquake, Japan, recorded by a new GPS buoy, *Earth Planets Space*, **57**, 297–301.
- Kawaguchi, K., Kaneko, S., Nishida, T. & Komine, T., 2015. Construction of the DONET real-time seafloor observatory for earthquakes and tsunami monitoring, in *Seafloor Observatories*, pp. 211–228, eds Favali, P. *et al.*, Springer.
- Kawai, H., Satoh, M., Kawaguchi, K. & Seki, K., 2012. The 2011 off the pacific coast of tohoku Earthquake Tsunami observed by the GPS buoys, seabed wave gauges, and coastal tide gauges of NOWPHAS on the Japanese Coast, in *Presented at the 22nd International Offshore and Polar Engineering Conference*, Rhodes, Greece, June 17–22.
- Kubo, A., Fukuyama, E., Kawai, H. & Nonomura, K., 2002. NIED seismic moment tensor catalogue for regional earthquakes around Japan: quality test and application, *Tectonophysics*, **356**, 23–48.
- Kubo, H., Nakamura, T., Suzuki, W., Kimura, T., Kunugi, T., Takahashi, N. & Aoi, S., 2018. Site amplification characteristics at Nankai seafloor observation network, DONET1, Japan, evaluated using spectral inversion, *Bull. seism. Soc. Am.*, **108**(3A), 1210–1218.
- Kubota, T., Hino, R., Inazu, D., Ito, Y. & Inuma, T., 2015. Complicated rupture process of the Mw 7.0 intraslab strike-slip earthquake in the Tohoku region on 10 July 2011 revealed by near-field pressure records, *Geophys. Res. Lett.*, **42**, 9733–9739.
- Kubota, T., Hino, R., Inazu, D., Ito, Y., Inuma, T., Ohta, Y., Suzuki, S. & Suzuki, K., 2017a. Coseismic slip model of offshore moderate interplate earthquakes on March 9, 2011 in Tohoku using tsunami waveforms, *Earth. Planet. Sci. Lett.*, **458**, 241–251.
- Kubota, T., Saito, T., Suzuki, W. & Hino, R., 2017b. Estimation of seismic centroid moment tensor using ocean bottom pressure gauges as seismometers, *Geophys. Res. Lett.*, **44**, 10907–10915.
- Maeda, T., Obara, K., Shinohara, M., Kanazawa, T. & Uehira, K., 2015. Successive estimation of a tsunami wavefield without earthquake source data: a data assimilation approach toward real-time tsunami forecasting, *Geophys. Res. Lett.*, **42**, 7923–7932.
- Matsumoto, H., Inoue, S. & Ohmachi, T., 2012. Dynamic response of bottom water pressure due to the 2011 Tohoku earthquake, *J. Disaster Res.*, **7**, 4698–4475.
- Matsumoto, K., Takanezawa, T. & Ooe, M., 2000. Ocean tide models developed by assimilating TOPEX/POSEIDON altimeter data into hydrodynamical model: a global model and a regional model around Japan, *J. Oceanogr.*, **56**, 567–581.
- Nakamura, T., Takahashi, N. & Suzuki, K., 2018. Ocean-bottom strong-motion observations in the Nankai Trough by the DONET real-time monitoring system, *Mar. Tech. Soc. J.*, **52**, 100–108, doi:10.4031/MTSJ.52.3.13.
- Nakano, M. *et al.*, 2018. The 2016 Mw 5.9 earthquake off the southeastern coast of Mie Prefecture as an indicator of preparatory processes of the next Nankai Trough megathrust earthquake, *Prog. Earth planet. Sci.*, **5**, 30.
- Okada, Y., 1992. Internal deformation due to shear and tensile faults in a half-space, *Bull. seism. Soc. Am.*, **82**, 1018–1040.
- Polster, A., Fabian, M. & Villinger, H., 2009. Effective resolution and drift of Paroscientific pressure sensors derived from long-term seafloor measurements, *Geochem. Geophys. Geosyst.*, **10**(8), Q08008.
- Saito, M., 1978. An automatic design algorithm for band selective recursive digital filters, *Butsuri Tanko*, **31**, 112–135 (in Japanese).
- Saito, T., 2013. Dynamic tsunami generation due to sea-bottom deformation: Analytical representation based on linear potential theory, *Earth Planets Space*, **65**, 1411–1423.
- Saito, T., 2017. Tsunami generation: validity and limitations of conventional theories, *Geophys. J. Int.*, **210**, 1888–1900.
- Saito, T., Inazu, D., Miyoshi, T. & Hino, R., 2014. Dispersion and nonlinear effects in the 2011 Tohoku-Oki earthquake tsunami, *J. geophys. Res.*, **119**, 5160–5180.

- Saito, T. & Tsushima, H., 2016. Synthesizing ocean bottom pressure records including seismic wave and tsunami contributions: Toward realistic tests of monitoring systems, *J. geophys. Res.: Solid Earth*, **121**, 8175–8195.
- Satake, K., 1989. Inversion of tsunami waveforms for the estimation of heterogeneous fault motion of large submarine earthquakes: The 1968 Tokachi-oki and 1983 Japan Sea earthquakes, *J. geophys. Res.*, **94**, 5627–5636.
- Satake, K., 1995. Linear and nonlinear computations of the 1992 Nicaragua earthquake tsunami, *Pure appl. Geophys.*, **144**, 455–470.
- Suzuki, K., et al., 2012. Seismicity near the hypocenter of the 2011 off the Pacific coast of Tohoku earthquake deduced by using ocean bottom seismographic data, *Earth Planets Space*, **64**, 1125–1135, doi:10.5047/eps.2012.04.010.
- Takagawa, T. & Tomita, T., 2014. Simultaneous inference of credible interval of inverted tsunami source and observation error by a hierarchical Bayes model, *J. Japan Soc. Civil Eng. Ser. B2 (Coastal Engineering)*, **70**(2), 1196–1200. (in Japanese with English abstract).
- Takahashi, M., 1981. Telemetry bottom pressure observation system at a depth of 2,200 meter, *J. Phys. Earth*, **29**, 77–88.
- Takemura, S., Kimura, T., Saito, T., Kubo, H. & Shiomi, K., 2018. Moment tensor inversion of the 2016 southeast offshore Mie earthquake in the Tonankai region using a three-dimensional velocity structure model: effects of the accretionary prism and subducting oceanic plate, *Earth Planets Space*, **70**, 50.
- Tanioka, Y., 2018. Tsunami simulation method assimilating ocean bottom pressure data near a tsunami source region, *Pure appl. Geophys.*, **175**, 721–729.
- Tatsumi, D., Calder, C.A. & Tomita, T., 2014. Bayesian near-field tsunami forecasting with uncertainty estimates, *J. geophys. Res.: Oceans*, **119**, 2201–2211.
- Titov, V.V., González, F.I., Bernard, E.N., Eble, M.C., Mofjeld, H.O., Newman, J.C. & Venturato, A.J., 2005. Real-time tsunami forecasting: challenges and solutions, *Nat. Hazards*, **35**, 35–41.
- Tsuji, T., Kamei, R. & Prat, G., 2014. Pore pressure distribution of a megasplay fault system in the Nankai Trough subduction zone: insight into up-dip extent of the seismogenic zone, *Earth. Planet. Sci. Lett.*, **396**, 165–178.
- Tsuji, T., Minato, S., Kamei, R., Tsuru, T. & Kimura, G., 2017. 3D geometry of a plate boundary fault related to the 2016 Off-Mie earthquake in the Nankai subduction zone, Japan, *Earth. Planet. Sci. Lett.*, **478**, 234–244.
- Tsushima, H., Hino, R., Fujimoto, H., Tanioka, Y. & Imamura, F., 2009. Near-field tsunami forecasting from cabled ocean bottom pressure data, *J. geophys. Res.*, **114**, B06309.
- Tsushima, H., Hino, R., Tanioka, Y., Imamura, F. & Fujimoto, H., 2012. Tsunami waveform inversion incorporating permanent seafloor deformation and its application to tsunami forecasting, *J. geophys. Res.*, **117**, B03311.
- Uehira, K. et al., 2016. Outline of seafloor observation Network for Earthquakes and Tsunamis along the Japan Trench (S-net), in *Abstract EGU2016-13832, Presented at EGU General Assembly 2016*, Vienna, Austria, April 17–22.
- Wallace, L.M. et al., 2016. Near-field observations of an offshore Mw 6.0 earthquake from an integrated seafloor and subseafloor monitoring network at the Nankai Trough, southwest Japan, *J. geophys. Res.: Solid Earth*, **121**, 8338–8351.
- Watts, D.R. & Kontoyiannis, H., 1990. Deep-Ocean bottom pressure measurement: drift removal and performance, *J. Atmos. Ocean. Technol.*, **7**, 296–306.
- Wells, D.L. & Coppersmith, K.J., 1994. New empirical relationships among magnitude, rupture length, rupture width, rupture area, and surface displacement, *Bull. seism. Soc. Am.*, **84**, 974–1002.
- Wessel, P. & Smith, W.H.F., 1998. New, improved version of generic mapping tools released, *EOS, Trans. Am. geophys. Un.*, **79**(47), 579.
- Yamamoto, N., Aoi, S., Hirata, K., Suzuki, W., Kunugi, T. & Nakamura, H., 2016a. Multi-index method using offshore ocean-bottom pressure data for real-time tsunami forecast, *Earth Planets Space*, **68**, 128.
- Yamamoto, N., Hirata, K., Aoi, S., Suzuki, W., Nakamura, H. & Kunugi, T., 2016b. Rapid estimation of tsunami source centroid location using a dense offshore observation network, *Geophys. Res. Lett.*, **43**, 4263–4269.

SUPPORTING INFORMATION

Supplementary data are available at *GJI* online.

Figure S1. Schematic illustration used to calculate Green's function for conventional and the time-derivative inversions.

Figure S2. Inversion results of the 2011 Off-Miyagi earthquake using synthetic OBP data containing artificial long-term trend; other explanations are same as those in Fig. 6.

Figure S3. Inversion results for the 2011 Off-Miyagi earthquake using synthetic OBP data containing small (5–10 hPa) artificial pressure offset changes; other explanations are same as those in Fig. 6.

Figure S4. Inversion results for the 2011 Off-Miyagi earthquake using synthetic OBP data containing large (30 hPa) artificial pressure offset change at station P06; other explanations are same as those in Fig. 6.

Figure S5. Trade-off curve between smoothing weight and VR, for (a) conventional inversion and (b) time-derivative inversion when analysing the Off-Mie earthquake. Grey lines denote weight of smoothing constraint adopted in this study.

Figure S6. Comparisons of (a) pressure waveforms and (b) time-derivative waveforms at DONET1 OBPs, and (c) pressure waveforms and (d) time-derivative waveforms at DONET2 OBPs for the 2016 Off-Mie earthquake between observed tsunami waveforms (black) and calculated waveforms calculated from tsunami source model with conventional inversion (blue) and time-derivative inversion (red) with OBP data apart from epicentre (Fig. 7). Observed waveforms drawn by thick black lines denote the time windows used in the inversion analysis. (e) Comparison of waveforms at coastal GPS buoys.

Figure S7. Tsunami source model of the 2016 Off-Mie earthquake obtained using (a) conventional and (b) time-derivative inversions without OBP data at KME18. Green contours denote tsunami source distribution obtained from analysis using OBP data apart from epicentre shown in Fig. 7(a). Other explanations are the same as those in Fig. 7.

Figure S8. Comparisons of waveforms for the 2016 Off-Mie earthquake between observed tsunami waveforms (black) and calculated waveforms calculated from tsunami source model with conventional inversion (blue) and time-derivative inversion (red), obtained from OBP data except for KME18 (Fig. S7); other explanations are the same as those in Fig. S6.

Figure S9. Comparisons waveforms for the 2016 Off-Mie earthquake between observed tsunami waveforms (black) and calculated waveforms calculated from tsunami source model obtained using all OBP data with time window from 1 to 5 min (Fig. 8). White background area denotes time window used for inversion. Note that scale of vertical axis is different from that in Figs S6e and S8e. Other explanations are the same as those in Fig. S6.

Figure S10. Schematic illustration of possible trade-off situation in simultaneous estimation of tsunami and linear trend; black line denotes observed tsunami waveform. It is possible to estimate the tsunami as a linear trend (blue dashed line), if tsunami data with a short time window are used (denoted by red arrow).

Please note: Oxford University Press is not responsible for the content or functionality of any supporting materials supplied by the authors. Any queries (other than missing material) should be directed to the corresponding author for the article.